



## Full length Article

# Characteristics of subevents and three-stage rupture processes of the 2015 Mw 7.8 Gorkha Nepal earthquake from multiple-array back projection

Weize Qin <sup>a,b</sup>, Huajian Yao <sup>a,b,\*</sup><sup>a</sup>Laboratory of Seismology and Physics of Earth's Interior, School of Earth and Space Sciences, University of Science and Technology of China, Hefei, Anhui 230026, China<sup>b</sup>National Geophysical Observatory at Mengcheng, Anhui, China

## ARTICLE INFO

## Article history:

Received 25 January 2016

Received in revised form 11 October 2016

Accepted 4 November 2016

Available online 5 November 2016

## Keywords:

Nepal earthquake

Back projection

High frequency seismic radiation

Subevents

Rupture process

## ABSTRACT

On 25 April 2015 an Mw 7.8 earthquake occurred in Nepal and caused about 9000 casualties. This earthquake ruptured part of the Main Himalaya Thrust fault, which is due to the convergence of the subducting Indian plate to the overriding Eurasian plate, and showed thrust mechanism with a very small fault dip angle (about 7–10°). We apply teleseismic multiple-array back projection analysis to study the rupture process of this earthquake and find 6 clear high frequency radiation sources (subevents). Our results illustrate a simple unilateral eastward rupture of ~160 km with relative stable rupture speed of ~2.8 km/s and a duration of 56 s. The entire rupture processes can be divided into 3 stages. The high frequency radiation appears to be mainly located at the edge of the large slip area, but the subevents have different characteristics in the western and eastern rupture areas. For this 2015 Nepal earthquake, the scales of asperities appear to be mainly controlled by depth, which dominates the overall patterns of slip and high frequency radiation. We finally propose a multiple-scale asperity model with stress and structural heterogeneities along the rupture direction to explain the distribution of high frequency subevents, co-seismic slip, and aftershocks.

© 2016 Elsevier Ltd. All rights reserved.

## 1. Introduction

The Tibetan Plateau is one of the most tectonically active areas in the world and it has been a research hotspot in the earth sciences for a long time. The collision of the Indian plate and Eurasian plate since 50 Myr ago is a consequence of the subduction of the Indian plate beneath Eurasia (Molnar and Tapponnier, 1975). Subsequently, The Indian plate continued to converge north-northeastward at a rate of ~36–40 mm/yr (Shen et al., 2000; Tapponnier et al., 2001; Wang et al., 2001). A fraction of convergence has been absorbed by crust shortening and thickening associated with the activation of the Main Himalaya Thrust fault (MHT) and a series of secondary faults including the Main Frontal Thrust fault (MFT), the Main Boundary Thrust (MBT), the Main Central Thrust (MCT), the southern Tibetan detachment (STD) (Fig. 1a). GPS observations and analyses illustrated a wide locking zone in the MHT along the collision zone of the Himalayan thrust belt

(Ader et al., 2012). The continuous loading of stress on the locking zone caused a large number of earthquakes inside this thrust zone, including many devastating ones in the past. Around the region of this Nepal Mw 7.8 earthquake, three mega earthquakes occurred in the past ~600 years, the 1505 Mw ~ 8.5 Lo Mustang earthquake (Bollinger et al., 2014), the 1934 Mw ~ 8.1 Nepal-Bihar earthquake (Ambraseys and Douglas, 2004), and the 1833 Mw ~ 7.6 Nepal earthquake (Bilham, 1995) (Fig. 1a). Because of the high plate convergence rate and rare occurrence of large earthquakes during the past decades, it was suggested that the risk of mega earthquakes should be alerted in the Nepal region (Bilham and Ambraseys, 2005; Bollinger et al., 2014).

The 25 April 2015 Mw 7.8 Gorkha Nepal earthquake is in control by the same thrust mechanism as the previous large events around this area, which occurred within the central Himalayan thrust belt (Fig. 1a). The epicenter of this earthquake is about 77 km northwest of Kathmandu, Nepal, and its rupture area is located in the gap between the rupture zone of the 1934 and 1505 mega earthquake, however, partly overlapping with the 1833 Nepal earthquake rupture region. It releases part of the stress and strain accumulated by the convergence of the plates. The Global Centroid Moment Tensor (GCMT) (Ekström et al., 2012) and the

\* Corresponding author at: Laboratory of Seismology and Physics of Earth's Interior, School of Earth and Space Sciences, University of Science and Technology of China, Hefei, Anhui 230026, China.

E-mail address: [hjyao@ustc.edu.cn](mailto:hjyao@ustc.edu.cn) (H. Yao).

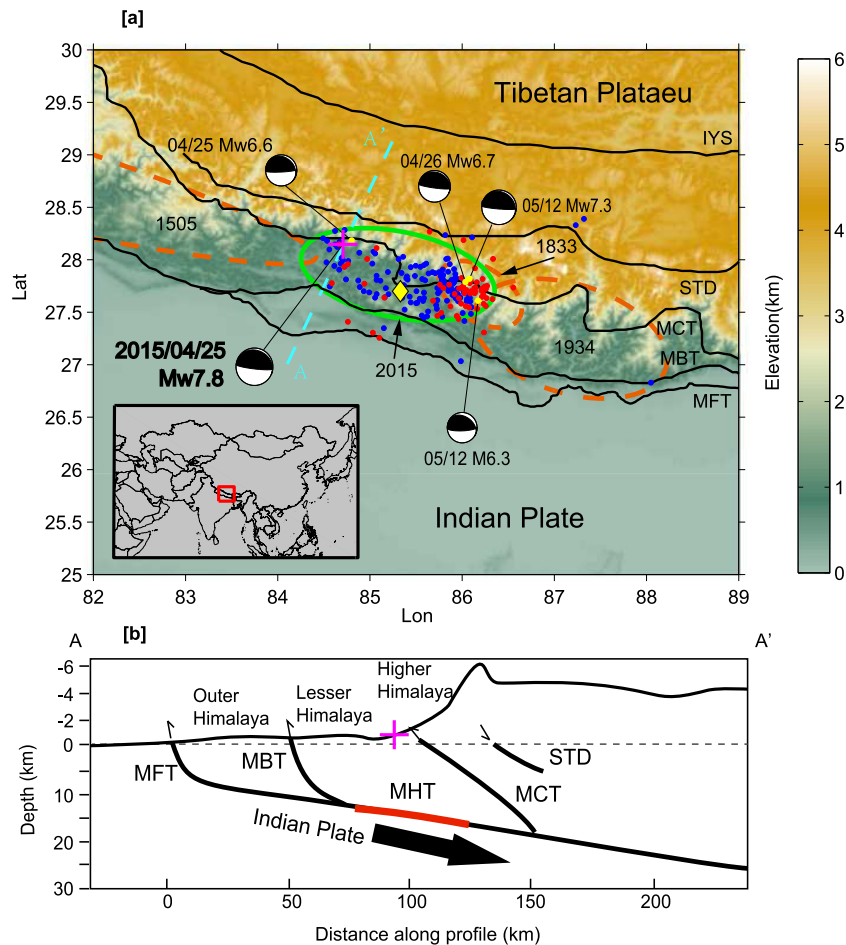


**Fig. 1.** (a) Topography and distribution of large earthquakes around the Nepal area. The purple cross gives the 2015 Gorkha Nepal earthquake epicenter (from USGS, [http://earthquake.usgs.gov/earthquakes/eventpage/us20002926#general\\_summary](http://earthquake.usgs.gov/earthquakes/eventpage/us20002926#general_summary)) and the yellow diamond gives the location of Kathmandu. Blue, red, and yellow dots are the aftershocks from 04/25/2015 to 05/30/2015. Among them, yellow dots are the large aftershocks with the moment tensor shown as the beach balls (from USGS), blue dots are the large aftershocks ( $M_w > 3.5$ ) between the main shock and the  $M_w 7.3$  aftershock on 05/12/2015, and red dots are the large aftershocks ( $M_w > 3.5$ ) after the  $M_w 7.3$  aftershock. The bold black lines are the main faults as mentioned in the main text. The brown ellipses describe the estimated rupture area of the 1505  $M_w \sim 8.2$ , 1833  $M_w \sim 8.1$ , and 1934  $M_w \sim 7.6$  events. The inset shows the location (red box) of the top figure. (b) Schematic vertical profile along AA' in (a) that shows the epicenter location (purple cross) and approximate rupture area (red line) of this Nepal earthquake. The fault geometry is approximately inferred from Pandey et al. (1995) and Bollinger et al. (2014). The topography data are from Amante and Eakins (2009). (For interpretation of the references to colour in this figure legend, the reader is referred to the web version of this article.)

settings of local geological structure favor a nodal plane with the strike of  $293^\circ$  and dip of  $7^\circ$ , and the finite-fault model from the United States Geological Survey (USGS) used a similar fault geometry (strike of  $290^\circ$  and dip of  $7^\circ$ ) ([http://earthquake.usgs.gov/earthquakes/eventpage/us20002926#scientific\\_tensor:us\\_us\\_20002926\\_mww](http://earthquake.usgs.gov/earthquakes/eventpage/us20002926#scientific_tensor:us_us_20002926_mww)). This implies that the Nepal earthquake occurred on the MHT, and the dominant rupture area is beneath the lower part of Lesser Himalaya (Fig. 1).

There are a number of studies published about the finite fault slip model and high frequency radiation of this Nepal earthquake (Aouac et al., 2015; Fan and Shearer, 2015; Galetzka et al., 2015; Grandin et al., 2015; Meng et al., 2016; Wang and Mori, 2016; Yagi and Okuwaki, 2015; Zhang et al., 2016). They all share similar results that the large slip area is located to the east of the epicenter, north of Kathmandu, the high frequency radiation appears at the northern edge of a large slip area, and the rupture speed is around 3 km/s. However, there are still some differences on the detailed distribution of fault slip and locations of high frequency seismic radiation. Fan and Shearer (2015), Wang and Mori (2016), Yagi and Okuwaki (2015), and Zhang et al. (2016) reported some changes in rupture speed in the beginning and terminating part of the rupture while others do not. Aouac et al. (2015) focused on the unzipping of the locking zone of the MHT,

while Grandin et al. (2015) emphasized the influence of structural architecture on the rupture behavior. Most of these studies agree that the area south of the rupture region or the shallow part of the MHT is still locked and the risk of earthquake hazards should be still alerted.

In this study we use teleseismic multiple-array back projection analysis to investigate the high-frequency seismic radiation and subevents distribution of the 2015 Nepal event. By comparing with the slip models and the distribution of the aftershocks, we propose a multi-asperity model with heterogeneous stress and structural anomaly distribution on the fault plane for this event after integration with regional geological and geophysical data.

## 2. Data and methods

The back projection method is widely used to investigate coseismic radiation of large earthquakes since the work by Ishii et al. (2005). This method assumes that the initial part of P waves is emitted from the epicenter and the later P wave trains are generated from the later rupture processes. The relative time shift of similar wave trains can be calculated by the multi-channel cross-correlation method (Vandecar and Crosson, 1990) and the adaptive stacking method (Rawlinson and Kennett, 2004; Yao et al., 2012),

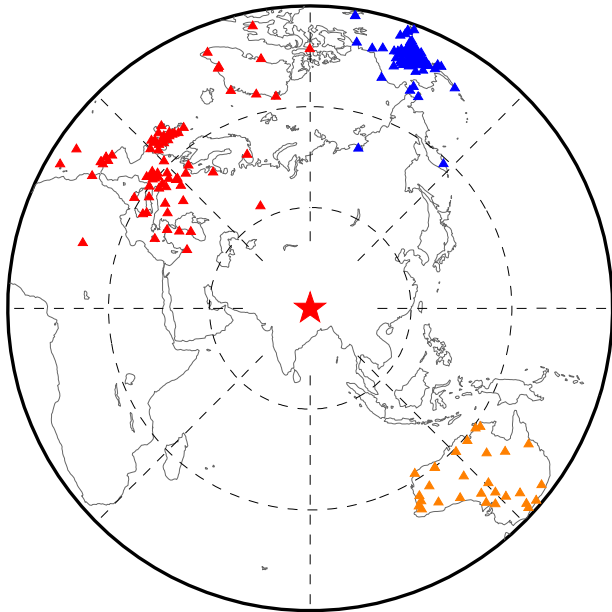


**Fig. 2.** The station distribution used in this study. The red triangles are the European (EU) stations, the blue triangles for the North American (NA) stations, and the orange triangles for the Australian (AU) stations. The dash lines are in 45° interval for azimuth and the dash circles are in 30° interval for epicentral distance. (For interpretation of the references to colour in this figure legend, the reader is referred to the web version of this article.)

and the location of the subevent is mainly determined by the relative time shifts observed at different stations (Yao et al., 2012).

We use data recorded at broadband seismometers from the Data Management Center (DMC) of Incorporated Research Institutions for Seismology (IRIS), including 101 stations from North America (NA), 74 from Europe (EU), and 29 from Australia (AU). The station distribution is shown in Fig. 2. For the AU and NA arrays, most of the stations are in the epicenter distance range of 60–90°. For the EU array, the epicenter distance is mainly within 40–80°. The azimuth coverage of the AU and NA arrays is around 40° and it's around 75° for the EU array. The data are first filtered to the frequency band of 0.05–4 Hz and then aligned by the initial 10 s of P waves, which were emitted from the hypocenter, using the cross-correlation method to eliminate the influence of 3D Earth structures on travel times (Ishii et al., 2005; Yao et al., 2012). We only keep the traces with correlation coefficients above 0.85 between each trace and their reference stack for the initial 10 s of P waves for later back projection analysis (Yao et al., 2012). The IASP91 model (Kennett and Engdahl, 1991) is used as the reference velocity model for the initial waveform alignment as well as for computing travel times from source grids to stations. After alignment, the data are then bandpass filtered to the target frequency band 0.5–4 Hz and normalized with their maximum amplitude. Due to waveform alignment, the results of back projection locations of energy bursts (subevents) are all relative to the epicenter.

The waveforms of the target frequency band from different arrays are shown in Fig. 3, which show clear differences of waveform amplitudes in the first 60 s. For the EU array, the first remarkable energy burst does not arise until 25 s, later than the NA and AU arrays. Meanwhile, the EU array appears to have the least separated pulse in the envelope and this feature is also seen in the result that will be discussed later.

We follow the process of Ishii et al. (2007), Yao et al. (2012), and Kiser and Ishii (2012) for the classical back projection analysis. The whole process can be summarized as

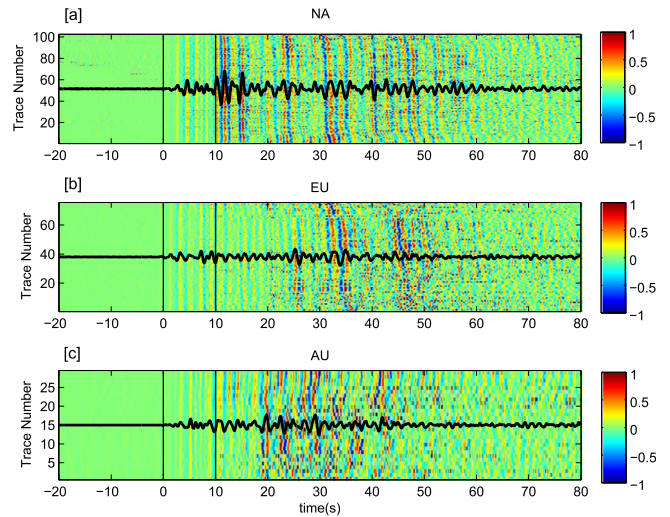


**Fig. 3.** The aligned waveforms in the frequency band 0.5–4 Hz from the NA (a), EU (b), and AU (c) array stations, respectively. The amplitude of each trace is normalized by the maximum amplitude within the time window 20 s before and 80 s after the P wave arrival for each array. The black wiggle is the linear stacked waveform of the aligned traces for each array. The two vertical lines in (a–c) indicate the first 10 s P wave window used for waveform alignment using cross-correlation.

$$V_{ij}(\theta, \varphi, t) \xrightarrow{\text{Back Projection}} S_i(x, y, t) \quad (1)$$

where  $V_{ij}$  is the velocity waveform of the  $j$ th station in the  $i$ th array,  $(\theta, \varphi)$  give the location of the station, and  $t$  is time.  $S_i$  is the raw stacked waveform, which is the slant stack of  $V_{ij}(\theta, \varphi, t)$ , and  $(x, y)$  are the grid coordinates in the source area. Since the use of the teleseismic P waves, we don't have depth resolution due to nearly vertical outgoing rays from the source region. Therefore,  $(x, y)$  are normally the horizontal grid coordinates at the focal depth. Instead of using the linear stacking scheme, here the  $n^{\text{th}}$ -root stacking method ( $n = 3$  here) (Rost and Thomas, 2002) is utilized in order to enhance the spatial and temporal resolution.

To guarantee the stability of the result, temporal smoothing process is usually applied to the raw stacked waveform  $S_i(x, y, t)$  using a sliding window averaging approach in order to obtain the smooth time-averaged back projection power  $P_i(x, y, t)$  (e.g. Yao et al., 2012). Then the summed power of multiple arrays is given by

$$P(x, y, t) = \sum_{i=1}^3 A_i P_i(x, y, t) \quad (2)$$

where  $A_i$  is the normalization factor. We define the time-dependent and spatially averaged power  $Q(t)$  or  $Q_i(t)$  as summation of  $P(x, y, t)$  (for the summed power of all arrays) or  $P_i(x, y, t)$  (for each array) over all spatial grids  $(x, y)$ .

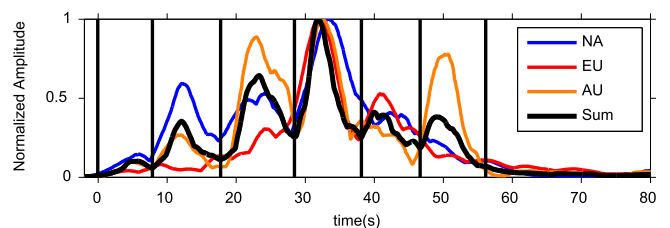


**Fig. 4.** Time-dependent and spatially averaged power (normalized) for each array (blue: NA, red: EU, orange: AU) and summed over all arrays (black). The summed power of all three arrays (black) illustrates 6 clear energy pulses as separated by the vertical lines. The last pulse can be only seen by the AU array, which may be due to radiation directivity. (For interpretation of the references to colour in this figure legend, the reader is referred to the web version of this article.)

### 3. Results

Fig. 4 shows the time-dependent and spatially averaged power for each array ( $Q_i(t)$ ) and summed over all arrays ( $Q(t)$ ), which gives six distinguishable pulses. Based on this, we divide the entire source radiation into 6 phases (time windows) shown as Fig. 5. The spatial- and time-averaged stack power of each array or summed over three arrays is given in Fig. 5, which illustrates 6 clear main energy bursts (subevents) within the time windows 0–8 s, 8–18 s, 18–28 s, 28–38 s, 38–47 s, and 47–56 s. The left three columns (except the bottom row) of Fig. 5 give the time-averaged power in different phases from each array, while the rightmost column of Fig. 5 gives the summed power from all 3 arrays. We perform

synthetic resolution tests using waveforms from an aftershock and demonstrate that the location errors of subevents are less than 10 km from our back projection analysis (see the [online supplementary material](#)).

The strongest energy radiation all appears in the 4th phase (28–38 s) from different array data. The location of the peak power moves basically along the strike line towards the southeast direction, which clearly demonstrates a unilateral rupture pattern of this earthquake. For the NA results, the energy bursts in the 2nd, 3rd, and 4th phases are strong and clear. The power of the energy burst in the 1st window is not large but the existence of this subevent is obvious. There are large-area and low-amplitude energy bursts in the 5th and 6th phases (38–56 s) of the NA results

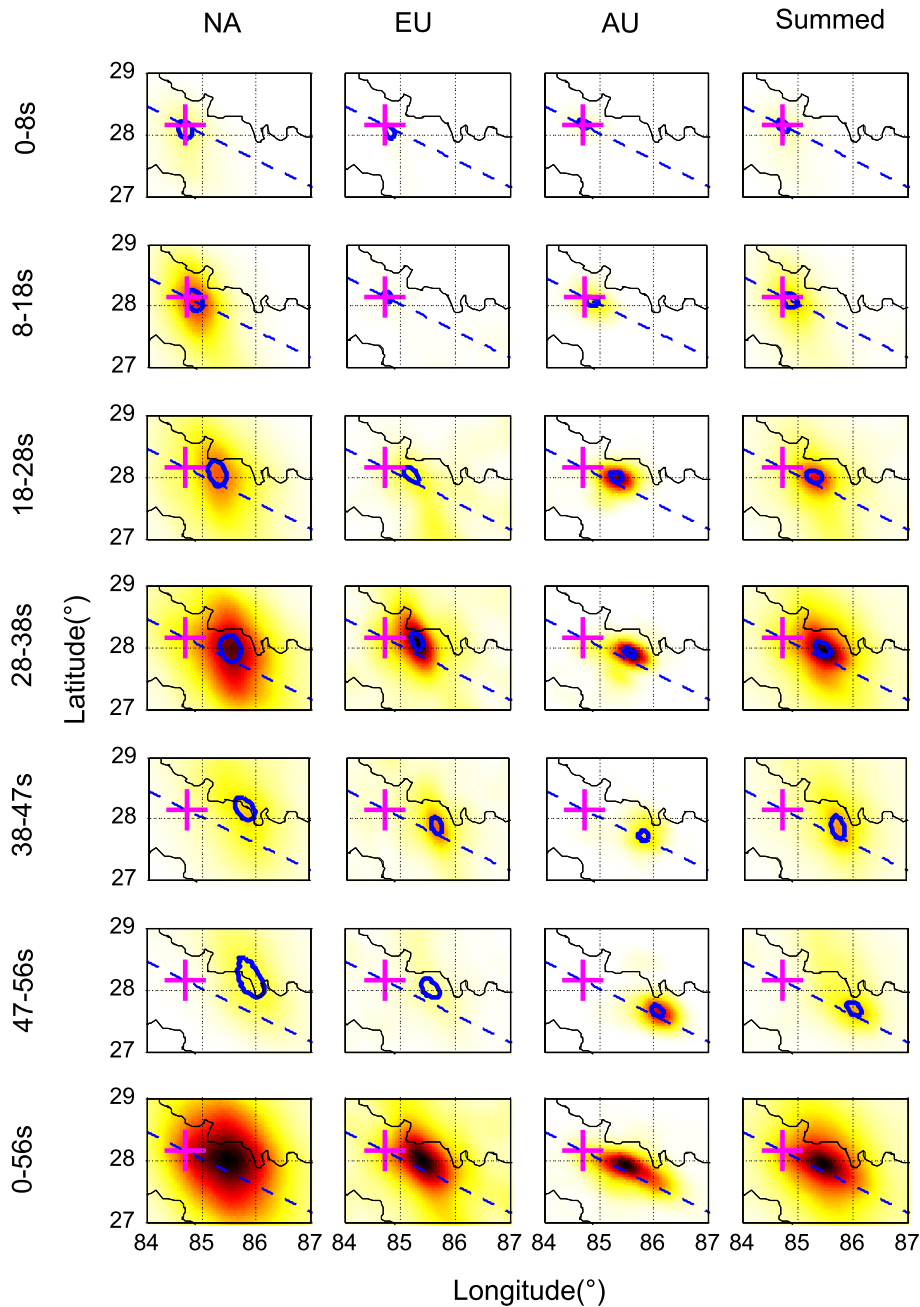


**Fig. 5.** Time-averaged power from back projection analysis of different arrays (left 3 columns) or summed over 3 arrays (4th column) within different time windows (phases). Each plot shows the stacked power within the corresponding time window (or phase) as indicated by the text left of each row. The power of each phase is normalized by the maximum power of the 4th phase (28–38 s). The power in the 7th row (0–56 s) is also normalized. The purple cross marks the epicenter location and the dashed blue line shows the strike (293°) of this Nepal event. The bold blue line gives the contour of 90% value of the peak power of each window. (For interpretation of the references to colour in this figure legend, the reader is referred to the web version of this article.)

**Table 1**

Subevent peak energy time, location, and relative power obtained from the summed back projection power of each phase (see last column in Fig. 5).

Subevent index	1	2	3	4	5	6
Time (s)	5.8	12.1	23.3	32.0	40.0	49.0
Longitude (°)	84.7079	84.8610	85.2693	85.4735	85.7287	86.0350
Latitude (°)	28.1473	28.0573	28.0123	27.9673	27.8323	27.6973
Normalized power	0.10	0.35	0.64	1.00	0.41	0.38

(Fig. 5), which appear more north than the locations of energy burst from the other two arrays in the same phase. The energy bursts in these last two phases seen by the NA array are not artifacts due to the array orientation as indicated by the results using the compressive sensing method (Yin et al., 2015).

For the EU array, the first two phases show very weak power and do not exist clear separation of each phase, which is consistent with the waveforms; the power in the 4th and 5th phases is strong. The results of the AU array hold the largest number of strong energy bursts (Figs. 4 and 5), especially the unique pulse with very large power in the 6th phase (47–56 s). If this subevent is an artifact, there is usually a stronger energy burst with similar shape and earlier time before this subevent. However, this is not observed here. This 6th subevent may be caused by radiation directivity that is well received by the AU array but not the other two arrays. However, its relative location to the hypocenter may be affected by local heterogeneity in the source region (Meng et al., 2016).

The different energy radiation patterns in different directions illustrate the necessity of handling data together from arrays in different orientations. The last row of Fig. 5 shows the summed power from the 3 different arrays. The summed results give a rupture length of ~160 km along strike. In comparison, the NA results show distinct seismic radiation north of the results from the EU and AU arrays in the last two phases (38–47 s and 47–56 s). This apparent difference may be caused by structural heterogeneity in the source region that is far away from the hypocenter. The EU and AU results are similar in shape and direction probably due to the reason that these two arrays are nearly on the opposite side with respect to the epicenter (Fig. 2). From the summed power, we pick the maximum energy point (referred as subevent) in each phase in Fig. 5. Table 1 gives the location, peak energy time, and relative energy of each subevent corresponding to each phase.

We project the subevent location to the strike direction (Fig. 6). Then the rupture speed can be estimated in the distance-time diagram. The subevent distribution is approximately on a straight line, which illustrates an average rupture speed of ~2.8 km/s. The rupture direction and speed from our results are similar to the results

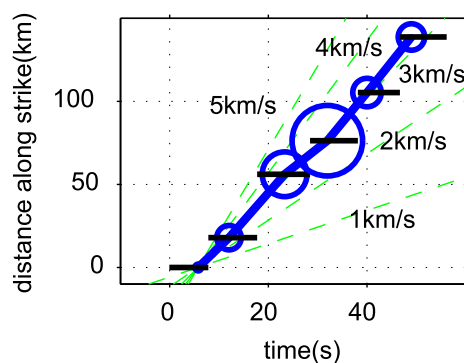


**Fig. 6.** Along strike and temporal distribution of subevents for rupture speed estimation. The circle indicates the time and distance of the subevents along strike. The area of each circle is proportional to the power of the corresponding subevent. The bold black lines mark the start and end time of the subevents and the dashed green lines are reference lines for rupture speed, from 1 km/s to 5 km/s with an interval of 1 km/s. (For interpretation of the references to colour in this figure legend, the reader is referred to the web version of this article.)

from other studies (e.g. Avouac et al., 2015; Liu and Ge, 2015; Meng et al., 2016; Wang and Mori, 2016; Yagi and Okuwaki, 2015; Zhang et al., 2016). The results of high frequency radiation are generally similar to previous studies (e.g. Avouac et al., 2015; Fan and Shearer, 2015; Grandin et al., 2015; Yagi and Okuwaki, 2015). However, our results have revealed most distinguishable high frequency subevents.

## 4. Discussion

### 4.1. Multiple-stage rupture processes

Our results from multiple-array back projection reveal 6-phase high-frequency energy radiation during the co-seismic unilateral rupture processes. Combining our results with the slip model from Avouac et al. (2015) and aftershocks distribution, we can divide the rupture processes into 3 stages (Fig. 7):

Stage 1: the 1st and 2nd phases (time windows 0–8 s and 8–18 s), which are the beginning of the rupture with weak high-frequency radiation, few aftershocks, and small co-seismic slip. Stage 2: the 3rd and 4th phases (time windows 18–28 s and 28–38 s), which is the main part of the rupture. Most accumulated stress and strain during the interseismic cycle are probably released in this stage. It is associated with strong high-frequency radiation, few aftershocks, and large co-seismic slip. Stage 3: the 5th and 6th phases (time windows 38–47 s and 47–56 s), which is the termination stage of the rupture with weak high-frequency radiation, many aftershocks, and small co-seismic slip.

A multiple-scale asperity model can explain most of the observation as follows. The western part of the rupture area (Zone I in Fig. 7a) has a small number of large asperities, and it has been mostly fractured during the main shock, denoted by large co-seismic slip and few aftershocks. The initiation of the rupture was accompanied with weak high-frequency radiation and the main part of the rupture was accompanied with strong seismic radiation. The middle part (Zone II in Fig. 7a) probably has a large number of small asperities, denoted by small co-seismic slip and many aftershocks. The 5th and 6th pulses (subevents) denote the termination of the rupture. These two pulses are much weaker in energy radiation and can be seen only by specific arrays (the EU and AU here). Recent Pg traveltimes tomography results (Pei et al., 2016) show that Zone I has fast upper crust P-wave velocities while Zone 2 shows apparent low velocity anomalies (Fig. 7a). And the 5th subevent is just located at the boundary between high and low velocity anomalies.

The aftershocks can be divided into two categories: the first-category aftershocks (blue dots in Figs. 1 and 7) are aftershocks that occurred between the Mw 7.8 main shock and the Mw 7.3 earthquake (Fig. 1), while the second-category aftershocks (red dots in Figs. 1 and 7) are aftershocks after the Mw 7.3 earthquake. The 5th pulse is in the region of the dense first-category aftershocks and the 6th pulse is possibly generated at the boundary between the first- and second-category aftershocks. This implies that the western part of the small-scale asperities (Zone II) was

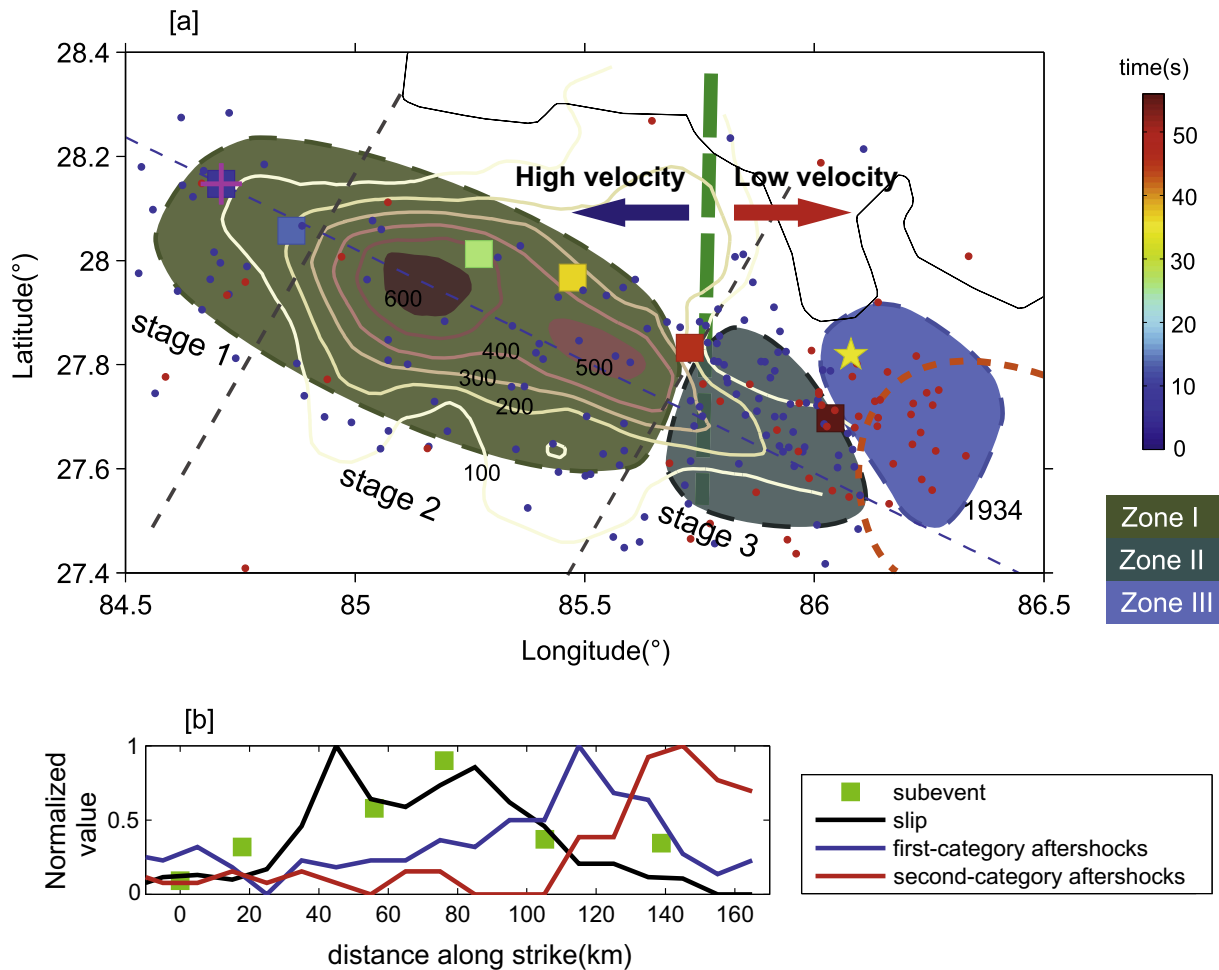


**Fig. 7.** (a) Rupture stages and schematic multiple-scale asperity model (three shaded regions) inferred from the distribution of high-frequency subevents (square, color for time), co-seismic slip (contour lines with unit in cm, from [Avouac et al. \(2015\)](#)), and aftershocks (dots, same as in [Fig. 1](#)). The thin black line is the national border line. The three shaded regions are the schematic representation of the three rupture zones. The dashed orange line gives the estimated western rupture limit of the 1934 event. The dashed black line is the schematic boundary between different rupture stages. The purple cross and dashed blue lines are the epicenter and strike direction of the Nepal event as in [Fig. 1](#), respectively. The green dashed line marks the sharp transition from high P-wave velocity (west) to low velocity (east) in the upper crust inferred from Pg travelttime tomography ([Pei et al., 2016](#)). (b) Along-strike normalized slip accumulation and the number of aftershocks for two different categories as defined in the main text. The values are computed in a 10 km distance interval. The subevents are shown as green squares, which are mainly on the margin of high slip area or transitional zone. (For interpretation of the references to colour in this figure legend, the reader is referred to the web version of this article.)

probably fractured during the main shock while the eastern part (Zone III) didn't fracture until the Mw 7.3 earthquake occurred 17 days later, which was due to the changes of stress state in the surrounding zone of the main shock area ([Wang et al., 2015](#)).

In combination with the approximate slip area of the 1934 earthquake ([Ambraseys and Douglas, 2004](#)), it can be inferred that the Mw 7.3 aftershock area (Zone III) is in a state of relative weak stress accumulation. Some of the accumulated stress has been released by the 1934 earthquake. This stress heterogeneity may dominate the termination of the Nepal main shock. This Nepal Gorkha earthquake area (Zone I) is in a high stress state and Zone II is the transition zone of stress state. The rupture stopped at the boundary of Zone II and Zone III, marked by the last subevent in our results. Nevertheless, the fracture of Zone I and II increases the stress of Zone III ([Wang et al., 2015](#)), and finally initiated the Mw 7.3 earthquake 17 days later as well as many aftershocks in Zone III.

#### 4.2. Relationship of co-seismic radiation, slip, aftershocks, and structure scales

Our results are generally consistent with the anti-correlation between areas of large co-seismic slip and strong high-frequency

radiation investigated in previous earthquake studies ([Allmann and Shearer, 2007](#); [Uchide et al., 2013](#)). Here we refer “structure” as an area with certain geometry and very similar physical property (e.g., frictional coefficient, rigidity). Generally speaking, larger scale structure tends to have lower natural frequency. The spectra of real earthquakes and theory of earthquake sources reveal that larger magnitude earthquakes tend to have lower corner frequencies (Aki and Richards, 2002). Dynamic simulation of earthquake rupture illustrates that variations both in frictional coefficients and fault geometries can cause high frequency radiation (Hu et al., 2014). These imply that with stable rupture speed, low frequency seismic radiation are dominantly generated by rupture of large-scale structures and high frequency energy bursts are generated by small-scale structures.

In order to analyze high frequency seismic radiation, the waveforms are usually bandpass filtered to a relatively high frequency band, e.g., 0.5–4 Hz in our study, 0.5–2 Hz in [Avouac et al. \(2015\)](#), and 0.2–3 Hz in [Fan and Shearer \(2015\)](#) for this Nepal event. While in the slip inversion studies for this Nepal earthquake, the frequency band is relatively low, e.g., 0.01–1 Hz in [Avouac et al. \(2015\)](#) and 0.001–0.36 Hz in [Yagi and Okuwaki \(2015\)](#), and the waveform fitting is typically dominated by lower frequency contents of the observed waveforms for large earthquakes. Because

frequency bands used in back projection and slip inversion are quite different, the corresponding patterns of seismic radiation and slip are usually not overlapping with each other. It has been also observed that high frequency radiation tends to originate at the edge of high-slip areas, for instance, for the 1998 Iwate (Mj 6.1) (Nakahara et al., 2002), the 2000 Tottori (Mw 6.6) (Suzuki and Iwata, 2009), the 2004 Parkfield (Mw 6.0) (Allmann and Shearer, 2007), and the 2010 El Mayor-Cucapah (Mw 7.2) (Uchide et al., 2013) earthquakes. The different distributions of high slip areas and high frequency radiation imply the differences in distributions of corresponding scale structures. The original structure scale dominates the distributions of slip and high frequency radiation patterns.

The rupture characteristics of the Mw 7.8 Nepal earthquake agrees well with the statement mentioned above. The high slip areas are adjacent to the high frequency radiation locations. The two regions with high slip are corresponding to two large-scale structures, and the high-frequency subevents are related to the adjacent smaller scale structures. The 1st subevent is the beginning of the rupture, the 2nd to the 5th subevents are approximately located at the northern margin of the large slip area, the 5th subevent is also in the sharp transitional region from high to low velocity anomalies, and the 6th subevent corresponds to the termination of the rupture. The distribution of co-seismic slip and aftershocks illustrates some spatial complementarity (Fig. 7), and the high-frequency subevents are either at the margin of large slip areas or in the region with small slip and dense aftershocks. For this Nepal earthquake, there may exist small-scale structural heterogeneities north of the large slip patches, for example, a ramp in fault geometry (Elliott et al., 2016) or frictional coefficient variation due to brittle-ductile transition at depths (Scholz, 1998). The along-strike sharp changes of upper crust structures, that is, from high velocity (or rigidity) in the west to low velocity (or rigidity) in the east, probably dominate the later stage of mainshock rupture and finally lead to the termination of the rupture.

Interestingly, high frequency radiation in the up-dip region (south of the large slip area) is not observed, similar to the observations of large subduction zone ruptures (e.g. Lay et al., 2012; Yao et al., 2013) in which high-frequency radiation is mainly located in the down-dip area of the subducting slab, although the mechanisms are possibly different due to differences in tectonic environments. The large slip area of this Nepal event corresponds to the previous interseismic locking zone (Ader et al., 2012; Avouac et al., 2015) while the high frequency radiation appears in the transition area of the locking zone and creeping zone, similar to the oceanic subduction environment (e.g. Lay et al., 2012; Yao et al., 2013), although the occurrence of this transition appears to be much shallower in the continental subduction regions (~15–20 km) than in the oceanic subduction regions (~30–45 km) due to differences in mineral contents in the crust (Scholz, 1998). The scales of asperities are mainly controlled by depth, which dominates the overall patterns of slip and high frequency radiation, while fault plane property and stress and structural heterogeneities along strike influence rupture behaviors in different stages for the Nepal event.

Therefore, the earthquake rupture process can be summarized as follows. The earthquake was initiated from a fracture of small-scale structure on the west side of a large-scale asperity and propagated to the east with an average speed of ~2.8 km/s. Some asperities in smaller scales on the north were fractured during the main rupture, leading to apparent high frequency radiation. The east side, which has low P-wave velocity anomaly in the upper crust, consists of a group of small-scale asperities with relatively weaker stress accumulation. The rupture was inhibited when propagating into this zone and finally stopped at the margin of the 1934 event rupture region, also generating high frequency

radiation at the rupture end. The fracture of Zone I increased the stress in Zone III, and triggered the Mw 7.3 earthquake and many other aftershocks. The observed patterns of high frequency radiation, slip distribution, and aftershock distribution are consistent with our model of multi-stage rupture processes of this Nepal earthquake sequence.

## 5. Conclusions

We utilized back projection analysis from 3 arrays of different directions to investigate high-frequency radiation patterns of the 2015 Nepal Gorkha earthquake. The co-seismic rupture can be divided into 6 phases each with a distinct high-frequency energy burst (subevent). The results illustrate a simple unilateral rupture of ~160 km from west to east with an average rupture speed of ~2.8 km/s and a rupture duration of 56 s. The high-frequency radiation subevents are mainly located at the edge of a large slip area, however, with different features in the western, middle, and eastern rupture regions. The scales of asperities are mainly controlled by depth, which dominates the overall patterns of slip and high frequency radiation. A multiple-scale asperity model with stress and structural heterogeneities along the rupture direction can well explain the distributions of high frequency subevents, co-seismic slip, and aftershocks.

## Acknowledgments

We appreciate the constructive comments from two anonymous reviewers that help to improve the original manuscript. We also thank Dr. Shengji Wei from Earth Observatory of Singapore (EOS) for providing the slip model and U.S. Geological Survey (USGS) for providing the earthquake catalog. All the waveform data are obtained from the Incorporated Research Institutions of Seismology (IRIS). This study is supported by National Natural Science Foundation of China (41374055) and the Fundamental Research Funds for the Central Universities (WK2080000053).

## Appendix A. Supplementary material

Supplementary data associated with this article can be found, in the online version, at <http://dx.doi.org/10.1016/j.jseaes.2016.11.012>.

## References

- Ader, T., Avouac, J.-P., Liu-Zeng, J., Lyon-Caen, H., Bollinger, L., Galetzka, J., Genrich, J., Thomas, M., Chanard, K., Sapkota, S.N., Rajaura, S., Shrestha, P., Ding, L., Flouzat, M., 2012. Convergence rate across the Nepal Himalaya and interseismic coupling on the Main Himalayan Thrust: implications for seismic hazard. *J. Geophys. Res.* – Solid Earth 117, B04403.
- Allmann, B.P., Shearer, P.M., 2007. A high-frequency secondary event during the 2004 Parkfield earthquake. *Science* 318, 1279–1283.
- Amante, C., Eakins, B.W., 2009. ETOPO1 1 Arc-Minute Global Relief Model: Procedures, Data Sources and Analysis. NOAA Technical Memorandum NESDIS NGDC-24. National Geophysical Data Center, NOAA, <http://dx.doi.org/10.7289/V5C8276M>.
- Ambraseys, N.N., Douglas, J., 2004. Magnitude calibration of north Indian earthquakes. *Geophys. J. Int.* 159, 165–206.
- Avouac, J.-P., Meng, L., Wei, S., Wang, T., Ampuero, J.-P., 2015. Lower edge of locked Main Himalayan Thrust unzipped by the 2015 Gorkha earthquake. *Nat. Geosci.* 8, 708–711.
- Billham, R., 1995. Location and magnitude of the 1833 Nepal earthquake and its relation to the rupture zones of contiguous great Himalayan earthquakes. *Curr. Sci.* 69, 101–128.
- Billham, R., Ambraseys, N., 2005. Apparent Himalayan slip deficit from the summation of seismic moments for Himalayan earthquakes, 1500–2000. *Curr. Sci.* 88, 1658–1663.
- Bollinger, L., Sapkota, S.N., Tapponnier, P., Klinger, Y., Rizza, M., Van der Woerd, J., Tiwari, D.R., Pandey, R., Bitri, A., de Berc, S.B., 2014. Estimating the return times of great Himalayan earthquakes in eastern Nepal: evidence from the Patu and Bardibas strands of the Main Frontal Thrust. *J. Geophys. Res.* – Solid Earth 119, 7123–7163.

- Ekström, G., Nettles, M., Dziewonski, A.M., 2012. The global CMT project 2004–2010: centroid-moment tensors for 13,017 earthquakes. *Phys. Earth Planet. Inter.* 200, 1–9.
- Elliott, J.R., Jolivet, R., González, P.J., Avouac, J.P., Hollingsworth, J., Searle, M.P., Stevens, V.L., 2016. Himalayan megathrust geometry and relation to topography revealed by the Gorkha earthquake. *Nat. Geosci.* 9, 174–180.
- Fan, W.Y., Shearer, P.M., 2015. Detailed rupture imaging of the 25 April 2015 Nepal earthquake using teleseismic P waves. *Geophys. Res. Lett.* 42, 5744–5752.
- Galetzka, J., Melgar, D., Genrich, J.F., Geng, J., Owen, S., Lindsey, E.O., Xu, X., Bock, Y., Avouac, J.P., Adhikari, L.B., Upreti, B.N., Pratt-Sitaula, B., Bhattarai, T.N., Sitaula, B.P., Moore, A., Hudnut, K.W., Szeliga, W., Normandeau, J., Fend, M., Flouzat, M., Bollinger, L., Shrestha, P., Koirala, B., Gautam, U., Bhattarai, M., Gupta, R., Kandel, T., Timsina, C., Sapkota, S.N., Rajauri, S., Maharjan, N., 2015. Slip pulse and resonance of the Kathmandu basin during the 2015 Gorkha earthquake, Nepal. *Science* 349, 1091–1095.
- Grandin, R., Vallée, M., Satriano, C., Lacassin, R., Klinger, Y., Simoes, M., Bollinger, L., 2015. Rupture process of the Mw = 7.9 2015 Gorkha earthquake (Nepal): insights into Himalayan megathrust segmentation. *Geophys. Res. Lett.* 42, 8373–8382.
- Ishii, M., Shearer, P.M., Houston, H., Vidale, J.E., 2005. Extent, duration and speed of the 2004 Sumatra-Andaman earthquake imaged by the Hi-Net array. *Nature* 435, 933–936.
- Ishii, M., Shearer, P.M., Houston, H., Vidale, J.E., 2007. Teleseismic P wave imaging of the 26 December 2004 Sumatra-Andaman and 28 March 2005 Sumatra earthquake ruptures using the Hi-net array. *J. Geophys. Res.* 112, B11307.
- Kennett, B.L.N., Engdahl, E.R., 1991. Traveltimes for global earthquake location and phase identification. *Geophys. J. Int.* 105, 429–465.
- Kiser, E., Ishii, M., 2012. Combining seismic arrays to image the high-frequency characteristics of large earthquakes. *Geophys. J. Int.* 188, 1117–1128.
- Lay, T., Kanamori, H., Ammon, C.J., Koper, K.D., Hutko, A.R., Ye, L.L., Yue, H., Rushing, T.M., 2012. Depth-varying rupture properties of subduction zone megathrust faults. *J. Geophys. Res. – Solid Earth* 117, B04311.
- Liu, Z.P., Ge, Z.X., 2015. Rupturing process of the Mw 7.9 Nepal earthquake inverted by the multi-array compressive sensing method. *Chinese J. Geophys. - Chinese Ed.* 58, 1891–1899.
- Meng, L., Zhang, A., Yagi, Y., 2016. Improving back projection imaging with a novel physics-based aftershock calibration approach: a case study of the 2015 Gorkha earthquake. *Geophys. Res. Lett.* 43, 628–636.
- Molnar, P., Tapponnier, P., 1975. Cenozoic tectonics of Asia: effects of a continental collision: features of recent continental tectonics in Asia can be interpreted as results of the India-Eurasia collision. *Science* 189, 419–426.
- Nakahara, H., Nishimura, T., Sato, H., Ohtake, M., Kinoshita, S., Hamaguchi, H., 2002. Broadband source process of the 1998 Iwate prefecture, Japan, earthquake as revealed from inversion analyses of seismic waveforms and envelopes. *Bull. Seismol. Soc. Am.* 92, 1708–1720.
- Pandey, M.R., Tandukar, R.P., Avouac, J.P., Lave, J., Massot, J.P., 1995. Interseismic strain accumulation on the Himalayan crustal ramp (Nepal). *Geophys. Res. Lett.* 22, 751–754.
- Pei, S., Liu, H., Bai, L., Liu, Y., Sun, Q., 2016. High-resolution seismic tomography of the 2015 Mw 7.8 Gorkha earthquake, Nepal: evidence for the crustal tearing of the Himalayan rift. *Geophys. Res. Lett.* 43, 9045–9052. <http://dx.doi.org/10.1002/2016GL069808>.
- Rawlinson, N., Kennett, B.L.N., 2004. Rapid estimation of relative and absolute delay times across a network by adaptive stacking. *Geophys. J. Int.* 157, 332–340.
- Rost, S., Thomas, C., 2002. Array seismology: methods and applications. *Rev. Geophys.* 40 (3), 1008.
- Scholz, C.H., 1998. Earthquakes and friction laws. *Nature* 391, 37–42.
- Shen, Z.K., Zhao, C.K., Yin, A., Li, Y.X., Jackson, D.D., Fang, P., Dong, D.N., 2000. Contemporary crustal deformation in east Asia constrained by Global Positioning System measurements. *J. Geophys. Res. – Solid Earth* 105, 5721–5734.
- Suzuki, W., Iwata, T., 2009. Broadband seismic wave radiation process of the 2000 western Tottori, Japan, earthquake revealed from wavelet domain inversion. *J. Geophys. Res. – Solid Earth* 114, B08302. <http://dx.doi.org/10.1029/2008jb006130>.
- Tapponnier, P., Zhiqin, X., Roger, F., Meyer, B., Arnaud, N., Wittlinger, G., Jingsui, Y., 2001. Oblique stepwise rise and growth of the Tibet plateau. *Science* 294, 1671–1677.
- Uchide, T., Yao, H.J., Shearer, P.M., 2013. Spatio-temporal distribution of fault slip and high-frequency radiation of the 2010 El Mayor-Cucapah, Mexico earthquake. *J. Geophys. Res. – Solid Earth* 118, 1546–1555.
- Vandecar, J.C., Crosson, R.S., 1990. Determination of teleseismic relative phase arrival times using multi-channel cross-correlation and least-squares. *Bull. Seismol. Soc. Am.* 80, 150–169.
- Wang, D., Mori, J., 2016. Short-Period Energy of the 25 April 2015 Mw 7.8 Nepal Earthquake Determined from Backprojection Using Four Arrays in Europe, China, Japan, and Australia. *Bull. Seismol. Soc. Am.* 106, 259–266.
- Wang, Q., Zhang, P.Z., Freymueller, J.T., Bilham, R., Larson, K.M., Lai, X., You, X.Z., Niu, Z.J., Wu, J.C., Li, Y.X., Liu, J.N., Yang, Z.Q., Chen, Q.Z., 2001. Present-day crustal deformation in China constrained by global positioning system measurements. *Science* 294, 574–577.
- Wang, W., Hao, J., He, J., Yao, Z., 2015. Rupture process of the Mw 7.9 Nepal earthquake April 25, 2015. *Sci. China Earth Sci.* 58, 1895–1900.
- Yagi, Y., Okuwaki, R., 2015. Integrated seismic source model of the 2015 Gorkha, Nepal, earthquake. *Geophys. Res. Lett.* 42, 6229–6235.
- Yao, H., Shearer, P.M., Gerstoft, P., 2012. Subevent location and rupture imaging using iterative backprojection for the 2011 Tohoku Mw 9.0 earthquake. *Geophys. J. Int.* 190, 1152–1168.
- Yao, H., Shearer, P.M., Gerstoft, P., 2013. Compressive sensing of frequency-dependent seismic radiation from subduction zone megathrust ruptures. *Proc. Natl. Acad. Sci.* 110, 4512–4517.
- Yin, J., Yao, H., Yang, H., 2015. Kinematic and dynamic rupture process of the 2015 Nepal Mw 7.8 earthquake. Abstract in the Fall Meeting of American Geophysical Union.
- Zhang, H., van der Lee, S., Ge, Z., 2016. Multiarray rupture imaging of the devastating 2015 Gorkha, Nepal, earthquake sequence. *Geophys. Res. Lett.* 43, 584–591.